Bubble dispenser in microfluidic devices

Thomas Cubaud, Mahidhar Tatineni, Xiaolin Zhong, and Chih-Ming Ho

Mechanical and Aerospace Engineering Department, University of California, Los Angeles, California 90095-1569, USA

This Brief Report presents experimental and computational results on bubble formation in microfluidic devices. Bubbles are generated at the right-angle intersection of four identical square microchannels. When the pressure gradient generated by the liquid flow dominates the pressure gradient generated by gas flow, the length of the produced confined bubbles follows a law based on the channel size and fluid volume fraction. This bubble production technique was used to produce monodisperse aqueous foam in two-dimensional and three-dimensional microchannels.

Great effort has been devoted in recent years to exploring multiphase flow in microgeometries [1–5]. Microfluidic devices are actively investigated in many scientific and industrial developments from micropower generation [6] to biochemical synthesis [7], and colloidal particle production [8]. Because of the delicate balance between geometrical constraints and dynamical surface tension effects, flowing multiphase fluids at the microscale present hysteretic properties. A critical issue for these systems is the production of well-defined capillary surfaces. Frequently used microfluidic devices consist of four crossed channels, this geometry, referred to as hydrodynamic focusing, was utilized to investigate phenomena as diverse as micromixing [9], DNA relaxation [10], and droplet formation [11–13].

Previous investigations on bubble formation in microgeometries were performed either in bulk fluid with circular orifices and capillaries [14,15] or in slit microchannels [16,17]. In this Brief Report, we investigate bubble formation in square microchannels and show that the compact confinement of a semi-infinite elongated bubble allows for its breakup by liquid cross flow in smaller bubbles, the length of which are equal to the ratio of the channel width to the liquid volumetric fraction.

Experiments were conducted with microchannels made of glass and silicon fabricated in a clean room environment. The fabrication steps include a selective deep reactive ion etching of a 100 μm double-sided polished silicon wafer at different depths. The four channels corresponding to the mixing chamber are etched through in a way to produce a square cross section. Pyrex glass pieces are anodic bonded to the top and the bottom of the etched-through silicon channel. A fiber light is placed at the other side of the channel to provide light for high-speed imaging (10 000 frames per second). Fluids are supplied to the device from pressurized reservoirs and flow rates are measured at the channel entrances with a volumetric mass flow meter for the liquid (Q_L) and a mass flow meter for the gas (Q_G). Because of the relative high pressure necessary to flow gas (from 1 to 3 atm) along with liquid through the device, volumetric gas flow rates Q_G were calculated at the device inlet. The two liquid channels are made equal in length and width and are connected upstream in a way to provide identical flow rates in both channels. Experiments in different channels were performed with water and

air (with a surface tension of $\gamma \sim 73$ mN/m) and with a mixture of water and sodium dodecyl sulfate (SDS) at 8 mM/l and air ($\gamma \sim 38$ mN/m).

Figure 1 represents processed experimental pictures of a water-air mixer in 100 μm square channels for different liquid and gas superficial velocities J_L and J_G ($J_i = Q_i/h^2$, where h represents both channel width and height). Gas flows in the central channel and liquid is injected from the side channels. We experimentally observed that the breakup occurs at the intersection of the four channels. Bubble size and distribution are a function of the liquid and gas flow rates. In a previous study [5], we showed that the homogeneous liquid fraction $\alpha_L = Q_L/(Q_L + Q_G)$ is a relevant parameter to characterize liquid-gas flow in microchannels. For different sets of liquid and gas flow rates (corresponding to a range of J_G from 0.01 to 1.1 m/s and J_L from 0.08 to 0.40 m/s), we measured the bubble length d as well as the length L between bubbles using image processing for $0.1 < \alpha_L < 1$. In Fig. 2,
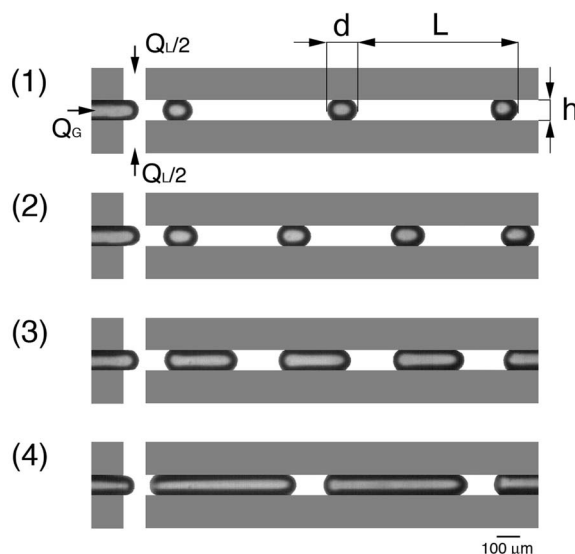

FIG. 1. Bubble formation for different water and air superficial velocities. (1) $J_L = 28.6$ cm/s, $J_G = 11.3$ cm/s, $\alpha_L = 0.72$; (2) $J_L = 26$ cm/s, $J_G = 19.3$ cm/s, $\alpha_L = 0.57$; (3) $J_L = 22$ cm/s, $J_G = 72.4$ cm/s, $\alpha_L = 0.23$; (4) $J_L = 18.1$ cm/s, $J_G = 109.9$ cm/s, $\alpha_L = 0.14$. Liquid inlet pressure was kept constant while gas inlet pressure was increased.
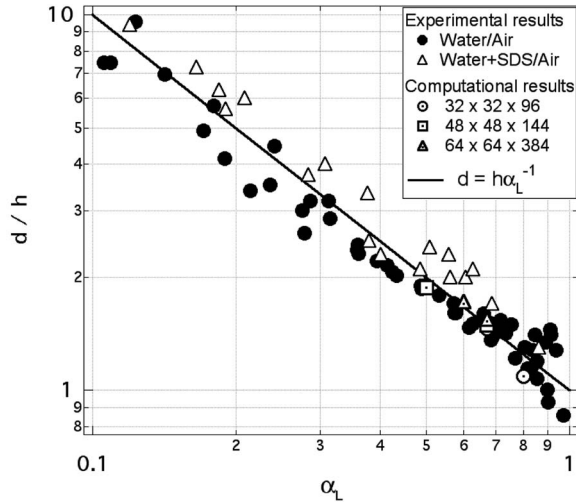
FIG. 2. Experimental and computational results on bubble length d as a function of homogeneous liquid fraction α_L.

we plotted the bubble length d, normalized by the square channel height h, as a function of the homogeneous liquid fraction α_L. Experimentally measured bubble lengths d collapse into as single curve that can be expressed as follows:

$$d = h\alpha_L^{-1}. \tag{1}$$

This empirical expression can be analytically deduced. For large liquid fractions $\alpha_L > 0.1$ ($Q_G/Q_L < 9$) and given the dynamic viscosity contrast between water and air ($\eta_L/\eta_G \sim 55$), the pressure gradient generated by the liquid flow ($\nabla P_L = A\eta_L Q_L/h^4$, with $A \approx 28.43$) at the intersection is larger than the one generated by the cylindrical gas flow ($\nabla P_G = 128\eta_G Q_G/\pi h^4$) at least by a factor of 4. Under these conditions and given the cylindrical shape of the gas thread, we can reasonably assume that the resistance offered by the gas for the liquid to flow across the intersection is negligible. Therefore, the time T necessary for the liquid to pinch the core gas bubble can be estimated by $T = h/J_L = h^3/Q_L$. We note that this scaling for the pinching time T is equivalent to the one assumed in circular geometries [14]. Also, recent experiments showed that the speed of collapse of a two-dimensional gas thread is proportional to the liquid velocity [17]. The bubble length d is proportional to the pinching time T and the average bubble velocity $J_B = (Q_L + Q_B)/h^2$ in a square channel [5], so we can estimate $d = J_B T$. One should note that Eq. (1) is specific to the square channel geometry. Indeed, it allows for the capillary surface to be confined as a cylinder, as opposed to slit channels, and it allows the liquid to flow in the wedges, as opposed to a circular channel. The breakup mechanism can be understood as the competition between the pressure drops generated by each flow. When the liquid pressure drop dominates, a very simple scaling law allows for the prediction of the bubble length [Eq. (1)]. For low $\alpha_L < 0.04$, the pressure drop generated by the gas flow is large enough to sustain the pressure drop generated by the liquid flow, and the flow becomes annular [5].

To further investigate the breakup phenomenon at high α_L, a level set numerical method was developed using a formulation based on a continuous surface tension model for two-phase flows. The discontinuity in pressure across the interface is set into a numerically continuous function. Level set based numerical methods are attractive for simulations of multiphase or multimaterial incompressible flows with complex topological changes [18–22]. The pressure jump conditions across the two-phase boundary can be considered explicitly via jump conditions or can be considered using a continuous model [20,21].

The governing equations are based on the incompressible Navier-Stokes equations in both fluids with jump conditions at the multiphase interface. In addition, the level set equation is also solved to keep track of the interface. The level set equation is as follows $\Phi_t + u \cdot \nabla\Phi = 0$. The variable Φ is positive in one fluid and negative in the other and the zero level set defines the interface between the two fluids. The velocities obtained from the Navier-Stokes equations are used to advance this level set variable according to the above equation. After every step, the function is reinitialized to the distance from the interface location. The details of the numerical method used and the validation cases were presented in Tatineni and Zhong [23]. The Navier-Stokes and level set equations are discretized on a standard maker and cell (MAC) grid with velocities on cell walls and the rest of the properties at the cell centers. A fifth order weighted essentially non-oscillatory (WENO) discretization [20] is used for the convective terms and a second order discretization is used for the viscous terms. A representation of the liquid-gas interface and the bubble pinching process in the numerical simulations is shown in Fig. 3.

The three-dimensional simulations were conducted for various gas and liquid flow rates to evaluate bubble size. The obtained bubble size for various liquid fraction values are compared with existing experimental results as shown in Fig. 2. The results show good agreement between numerical simulations and experimental results. The numerical results are found to be within the experimental scatter. In addition, for each liquid fraction value three grid sizes were used to evaluate the grid independence of the results obtained. Bubble length is essentially grid independent.

Another important parameter of the phenomenon is the bubble distribution, customizable using the distance L between the bubbles. The shape of a flowing elongated bubble in a square microchannel differs from a cylinder. The film thickness between the bubble and the solid walls depends on the capillary number Ca, as well as the quantity of liquid in the corners [24]. In the mixing chamber, measured bubble velocity J_B (from 0.15 to 1.3 m/s) is always much larger than the dewetting speed $U_{\text{dew}} \approx 7$ mm/s, associated with the hydrophilic channel walls [5], so bubbles are constantly lubricated. When surfactant is present, viscous friction causes it to accumulate at the rear of the bubble, inducing a gradient of surface tension responsible for a slight bubble deformation compared to the nonsurfactant case. In both cases, a first order approximation would neglect the bubble curvature, as well as the liquid flowing in the corner and in the thin film. By doing so, the bubble shape can be assumed as a rectangular plug of volume dh^2. Along with the plug approxima-
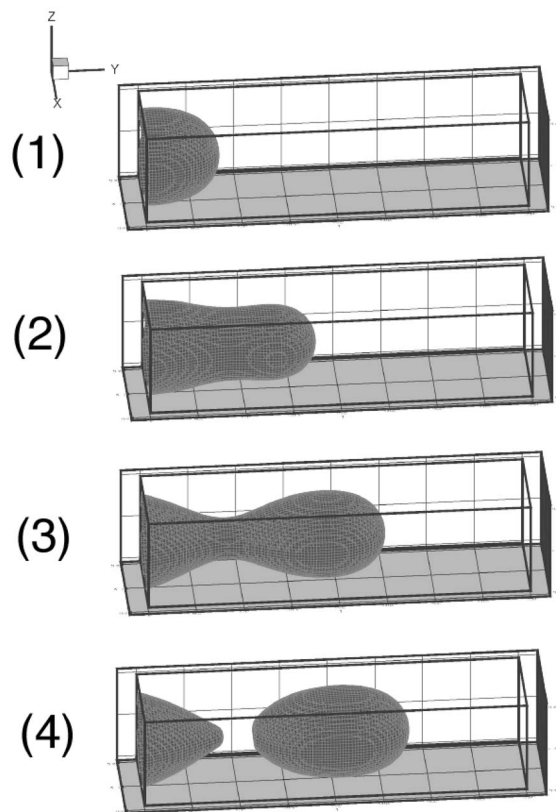
FIG. 3. Results from numerical simulations using the level set method showing the formation of the gas bubble due to pinching by the liquid cross flow ($J_L=88$ cm/s, $J_G=44$ cm/s, $\alpha_L \approx 0.67$, $d/h \approx 1.5$).

tion, volume conservation allows estimating the distance L between bubbles by writing $1-\alpha_L=d/L$ combined with Eq. (1). The distance L between bubbles can be expressed as a function of the bubble length d, $L/h=(d/h)^2/(d/h-1)$. As can be seen in Fig. 4, experimental data agree fairly well with the prediction for large bubble length $d>4h$. The distance between bubbles is minimal when the liquid flow rate
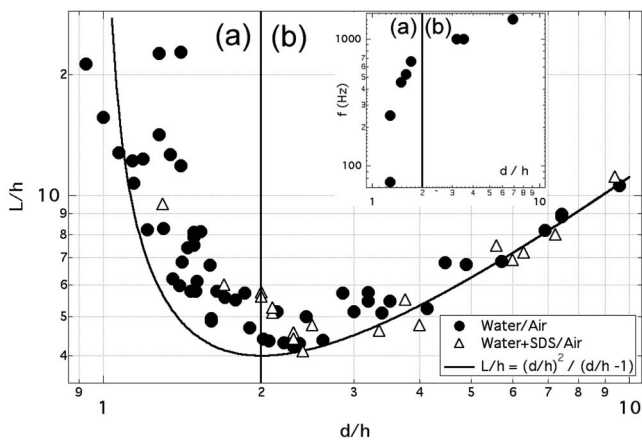

FIG. 4. Evolution of the distance L between bubbles as a function of bubble length d. Region of bubble formation: (a) pseudoconstant volume and (b) pseudoconstant frequency.

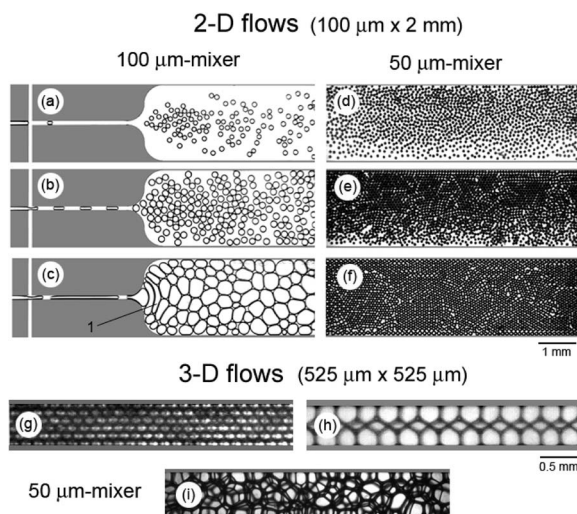

2-D flows (100 μm × 2 mm)

3-D flows (525 μm × 525 μm)

FIG. 5. Aqueous foam flow generated in different geometries with an on-chip liquid-gas mixer. (a) $\alpha_L \sim 0.91$; (b) $\alpha_L \sim 0.57$; (c) $\alpha_L \sim 0.09$; (d) $\alpha_L \sim 0.47$; (e) $\alpha_L \sim 0.30$; (f) $\alpha_L \sim 0.20$; (g) $\alpha_L=0.11$; (h) $\alpha_L \sim 0.01$; (i) $\alpha_L \sim 0.06$. Polydispersity observed in (c) is the result of bubble break during the flow such as indicated with Eq. (1). Three-dimensional flow exhibits ordered and disordered structures.

equals the gas flow rate ($Q_L=Q_G$), corresponding to a bubble length $d/h=2$. At this point the liquid length between the bubbles is equal to the bubble length.

The bubble formation presented in this Brief Report is somewhat analogous to the classical problem of bubble formation at an orifice [25]. In this situation, for low gas flow rates, the bubble volume remains essentially constant and the frequency of bubble production is proportional to the gas flow rate. This type of formation is referred to as constant volume. For larger flow rates, the bubble frequency levels off to a constant value and the volume increases in proportion to the gas flow rate. This type of formation is referred to as constant frequency. In our system, when $d<2h$, we also observe a pseudoconstant-volume regime where the bubble volume slightly increases as the frequency increases [Figs. 1(a) and 1(b) and Fig. 4]. For $d>2h$, the frequency slightly increases as the bubble volume increases (Fig. 4).

This bubble nucleation technique is particularly attractive to produce well-defined complex multiphase flows such as aqueous foam in confined systems. In this case, the production of a monodisperse array of bubbles is advantageous for foam generation where monodispersity is a factor of longevity, as coarsening (Ostwald ripening) occurs between bubbles of different sizes. We experimentally produced and flowed aqueous foam made of a mixture of water and SDS at 8 mM/l and air in two-dimensional and three-dimensional microchannels incorporating an on-chip bubble dispenser (Fig. 5).

For two-dimensional flows (0.1 mm × 2 mm), we investigated the influence of two mixing channel heights $h=100$ μm [Figs. 5(a)–5(c), mixing sections are shown on the left] and $h=50$ μm [Figs. 5(d)–5(f)]. As surfactant molecules, to some extent, prevent bubbles from coalescence,

the produced flows differ in bubble size for equivalent liquid fractions. Polydispersity observed in Fig. 5(c) is due to bubble rupturing caused by cooperation between shear, bubble concentration, and sudden channel expansion from the mixing chamber to the larger channel. Of particular interest, we investigated aqueous foam flow in three-dimensional channels (525 μm$\times$525 μm) as can be seen in Figs. 5(g)–5(i). As the ratio of the main channel height and the mixing chamber height ($w/h \sim 10$) is relatively high, a large variety of flows is observed. Flow patterns displayed in Fig. 5 correspond to liquid fractions below the compact hexagonal packing of spherical objects ($\alpha_L \approx 0.26$). Bubbles form a compact arrangement of polyhedral cells and flow as a rigid body with a liquid lubrication layer on the walls. The flows display ordered [(g) and (h)] and disordered [(i)] structures. Experiments in microchannels with surface modifica-tions (hydrophilic and/or hydrophobic) show a rich collection of complex flow patterns [26], notably by introducing three-phase contact lines.

In summary, we demonstrated that compact three-dimensional hydrodynamic focusing in square microchannels allows for the production of a monodisperse array of bubbles. When the pressure drop generated by the liquid flow dominates, the size of the produced bubbles is shown to depend on the channel size and the liquid volumetric fraction. This mixer was used to produce monodisperse aqueous foam in microchannels. This production technique is very promising in the development of complex multiphase material, such as cellular material at room temperature.

[1] R. S. Stanley, R. F. Barron, and T. A. Amee, *1997 Micro-electrochemical Systems (MEMS)*, Dallas, 1997, edited by C. J. Kim *et al.* (American Society of Mechanical Engineers, New York, 1997), Vol. 354.

[2] T. Thorsen, R. W. Roberts, F. H. Arnold, and S. R. Quake, Phys. Rev. Lett. **86**, 4163 (2001).

[3] T. S. Zhao and Q. C. Bi, Int. J. Multiphase Flow **27**, 765 (2001).

[4] R. Dreyfus, P. Tabeling, and H. Willaine, Phys. Rev. Lett. **90**, 144505 (2003).

[5] T. Cubaud and C.-M. Ho, Phys. Fluids **16**, 4575 (2004).

[6] T. J. Yen, X. Zhang, G. Q. Lu, and Y. Wang, Appl. Phys. Lett. **83**, 4056 (2003).

[7] B. Zheng, J. D. Tice, and R. F. Ismagilov, Adv. Mater. (Weinheim, Ger.) **16**, 15 (2004).

[8] S. A. Khan, A. Gunther, M. A. Smidt, and K. F. Jensen, Langmuir **20**, 8604 (2004).

[9] J. B. Knight, A. Vishwanath, J. P. Brody, and R. H. Austin, Phys. Rev. Lett. **80**, 3863 (1998).

[10] P. K. Wong, Y. K. Lee, and C.-M. Ho, J. Fluid Mech. **497**, 55 (2003).

[11] S. L. Anna, N. Bontoux, and H. A. Stone, Appl. Phys. Lett. **82**, 3 (2002).

[12] D. R. Link, S. L. Anna, D. A. Weitz, and H. A. Stone, Phys. Rev. Lett. **92**, 054503 (2004).

[13] J. D. Tice, H. Song, A. D. Lyon, and R. F. Ismagilov, Langmuir **19**, 9127 (2003).

[14] A. M. Ganan-Calvo and J. M. Gordillo, Phys. Rev. Lett. **87**, 274501 (2001).

[15] A. M. Ganan-Calvo, Phys. Rev. E **69**, 027301 (2004).

[16] J. M. Gordillo, Z. Cheng, A. M. Ganan-Calvo, M. Marquez, and D. A. Weitz, Phys. Fluids **16**, 2828 (2004).

[17] P. Garstecki, H. A. Stone, and G. M. Whitesides, Phys. Rev. Lett. **94**, 164501 (2005).

[18] M. Sussman, P. Smereka, and S. Osher, J. Comput. Phys. **114**, 146 (1994).

[19] Y. C. Chang, T. Y. Hou, B. Merriman, and S. Osher, J. Comput. Phys. **124**, 449 (1996).

[20] R. Fedkiw, T. Aslam, B. Merriman, and S. Osher, J. Comput. Phys. **152**, 457 (1999).

[21] M. Kang, R. Fedkiw, and X-D. Liu, J. Sci. Comput. **15**, 323 (2000).

[22] M. Sussman and E. G. Puckett, J. Comput. Phys. **162**, 301 (2000).

[23] M. Tatineni and X. Zhong, AIAA Paper 2004-0929 (2004).

[24] H. Wong, C. J. Radke, and S. Morris, J. Fluid Mech. **292**, 71 (1995).

[25] R. S. Brodkey, *The Phenomena of Fluid Motions* (Addison-Wesley, Reading, MA, 1967).

[26] T. Cubaud, U. Ulmanella, and C.-M. Ho, *5th International Conference on Multiphase Flow*, Yokohama, 2004, edited by Y. Matsumoto *et al.* (to be published).